Density-driven defect-mediated network collapse of GeSe₂ glass

Kamil Wezka,[1,*] Assil Bouzid,[2,*] Keiron J. Pizzey,[1] Philip S. Salmon,[1,†] Anita Zeidler,[1] Stefan Klotz,[3] Henry E. Fischer,[4] Craig L. Bull,[5] Matthew G. Tucker,[5] Mauro Boero,[2] Sébastien Le Roux,[2] Christine Tugène,[2] and Carlo Massobrio[2]

[1]*Department of Physics, University of Bath, Bath BA2 7AY, United Kingdom*
[2]*IPCMS, 23 rue du Loess, BP 43, F-67034 Strasbourg Cedex 2, France*
[3]*IMPMC, CNRS UMR 7590, Université Pierre et Marie Curie, F-75252 Paris, France*
[4]*Institut Laue-Langevin, 6 rue Jules Horowitz, BP 156, F-38042 Grenoble Cédex 9, France*
[5]*ISIS Facility, Rutherford Appleton Laboratory, Chilton, Didcot, Oxon OX11 0QX, United Kingdom*

The evolution in structure of the prototypical network-forming glass GeSe₂ is investigated at pressures up to ∼16 GPa by using a combination of neutron diffraction and first-principles molecular dynamics. The neutron diffraction work at pressures ⩽8.2 GPa employed the method of isotope substitution, and the molecular dynamics simulations were performed with two different exchange-correlation functionals, the Becke-Lee-Yang-Parr (BLYP) and the hybrid Heyd-Scuseria-Ernzerhof HSE06. The results show density-driven structural transformations that differ substantially from those observed in common oxide glasses such as SiO₂ and GeO₂. Edge-sharing tetrahedra persist as important structural motifs until a threshold pressure of ∼8.5 GPa is attained, whereupon a mediating role is found for homopolar bonds in the appearance of higher coordinated Ge-centered polyhedra. These mechanisms of network transformation are likely to be generic for the class of glass-forming materials where homopolar bonds and fragility-promoting edge-sharing motifs are prevalent in the ambient-pressure network.

I. INTRODUCTION

The density-driven structural transformations in network-forming glasses lead to changes in their physicochemical properties that can be abrupt as in so-called polyamorphic transitions [1,2]. The mechanisms of densification will depend on the network topology and, since this is governed by the chemical-bonding scheme, chalcogenide glasses are anticipated to exhibit different behavior to their oxide counterparts. For example, the ability of chalcogenide glasses to form at nonstoichiometric compositions [3] points to flexibility in character of the network-forming structural motifs, i.e., to enhanced structural variability [4,5]. A prototype is provided by glassy GeSe₂ where the ambient-pressure network, built from a mixture of corner-sharing (CS) and edge-sharing (ES) tetrahedra, incorporates a significant number of Ge-Ge and Se-Se homopolar bonds [6–15]. The nature of the density-driven network collapse is, however, uncertain. Different studies at pressures P up to ∼9 GPa find either (i) a continuous structural change [16,17] or (ii) a discontinuous semiconductor-glass to metal-crystalline transition [18,19].

In this paper we use *in situ* high-pressure neutron diffraction to investigate the structure of GeSe₂ glass under compression from ambient pressure to P ∼16 GPa at room temperature (T ∼ 300 K). Enhanced information is accessed by applying the isotope substitution method to disentangle the complexity of correlations associated with a single diffraction pattern [20]. The experimental work is complemented by a set of Car-Parrinello [21] first-principles molecular dynamics (FPMD) simulations [15,22–24]. This approach is necessitated by the presence of homopolar bonds, which preclude any reliable

modeling based on interatomic potentials [25]. The combined techniques yield a self-consistent picture at a pressure below ∼8.5 GPa in which there is no change to the mean nearest-neighbor coordination number $\bar{n}$ but an interplay between the fractions of CS versus ES tetrahedra. At pressures beyond this threshold, however, the diffraction and FPMD results follow different pathways of metastability. This outcome is likely to originate from different thermal histories, with the simulations showing an increase of $\bar{n}$ with pressure that is more rapid than found in experiment. In the simulations, further densification proceeds by the formation of higher-coordinated Ge and Se atoms where, on initial formation, large proportions of these higher-coordinated atoms form homopolar bonds. These defects in the chemical ordering therefore play a mediating role in the structural transformation of the modeled glass structure.

The paper is organized as follows. The essential theory for the neutron diffraction experiments is given in Sec. II. The experimental and FPMD methods are then described in Secs. III and IV, respectively. The results are presented in Sec. V and the mechanisms of network collapse are discussed in Sec. VI. Conclusions are drawn in Sec. VII.

II. THEORY

In a neutron diffraction experiment on GeSe₂ glass, the total structure factor

$$F(k) = \sum_\alpha \sum_\beta c_\alpha c_\beta b_\alpha b_\beta [S_{\alpha\beta}(k) - 1] \qquad (1)$$

is measured, where α and β denote the chemical species, c_α and b_α represent the atomic fraction and coherent neutron scattering length of chemical species α, $S_{\alpha\beta}(k)$ is a partial structure factor, and k is the magnitude of the scattering vector [26]. Let diffraction experiments be performed under the same conditions on two isotopically enriched samples of $^{70}\text{Ge}^{\text{N}}\text{Se}_2$ and $^{73}\text{Ge}^{76}\text{Se}_2$, where N denotes the natural

---

isotopic abundance, yielding the functions $^{70}_{N}F(k)$ and $^{73}_{76}F(k)$, respectively. Then, the Se-Se correlations can be eliminated by the combination

$$\Delta F_{Ge}(k) \equiv {}^{70}_{N}F(k) - \left(b^2_{NSe}/b^2_{76Se}\right) {}^{73}_{76}F(k)$$
$$= A[S_{GeSe}(k) - 1] + B[S_{GeGe}(k) - 1], \quad (2)$$

where $A = 2c_{Ge}c_{Se}(b_{70Ge}b_{NSe} - b^2_{NSe}b_{73Ge}/b_{76Se})$ and $B = c^2_{Ge}(b^2_{70Ge} - b^2_{NSe}b^2_{73Ge}/b^2_{76Se})$. Alternatively, the Ge-Ge correlations can be eliminated by the combination

$$\Delta F_{Se}(k) \equiv {}^{73}_{76}F(k) - \left(b^2_{73Ge}/b^2_{70Ge}\right) {}^{70}_{N}F(k)$$
$$= C[S_{GeSe}(k) - 1] + D[S_{SeSe}(k) - 1], \quad (3)$$

where $C = 2c_{Ge}c_{Se}(b_{73Ge}b_{76Se} - b^2_{73Ge}b_{NSe}/b_{70Ge})$ and $D = c^2_{Se}(b^2_{76Se} - b^2_{73Ge}b^2_{NSe}/b^2_{70Ge})$.

The real-space information is obtained by Fourier transformation, e.g., the total pair-distribution function is given by

$$G(r) = \frac{1}{2\pi^2 \rho r} \int_0^\infty dk\, k\, F(k) M(k) \sin(kr), \quad (4)$$

where r is a distance in real space, ρ is the atomic number density of the glass, and $M(k)$ is a modification function defined by $M(k) = 1$ for $k \leqslant k_{max}$, $M(k) = 0$ for $k > k_{max}$. The latter is introduced because a diffractometer can measure only over a finite range up to a maximum value k_{max}. However, if k_{max} is sufficiently large that $F(k)$, $\Delta F_{Ge}(k)$, and $\Delta F_{Se}(k)$ no longer show structure at high k, then the corresponding real-space functions $G(r)$, $\Delta G_{Ge}(r)$, and $\Delta G_{Se}(r)$ are obtained from Eqs. (1)–(3), respectively, by replacing each $S_{\alpha\beta}(k)$ by its corresponding partial pair-distribution function $g_{\alpha\beta}(r)$. To facilitate a comparison between the FPMD and diffraction results, the reciprocal-space functions constructed from the simulations were Fourier transformed with k_{max} set at the experimental value. The severity of Fourier transform artifacts can be reduced by using a Lorch [27] modification function, albeit at the expense of a broadening of sharp peaks in the real-space functions, where $M(k) = \sin(ak)/(ak)$ for $k \leqslant k_{max}$, $a \equiv \pi/k_{max}$, and $M(k) = 0$ for $k > k_{max}$ [28].

The mean nearest-neighbor coordination number is defined by $\bar{n} \equiv c_{Ge}[\bar{n}^{Ge}_{Ge} + \bar{n}^{Se}_{Ge}] + c_{Se}[\bar{n}^{Se}_{Se} + \bar{n}^{Ge}_{Se}]$ where $\bar{n}^\beta_\alpha$ is the mean coordination number for chemical species β around chemical species α. $\bar{n}$ can be extracted by integrating over the first peak in the so-called Bhatia-Thornton number-number partial pair-distribution function $g_{NN}(r)$, which can be measured accurately by performing a neutron diffraction experiment on a sample of $^{N}Ge^{N}Se_2$ because $b_{NGe} \simeq b_{NSe}$ [12].

III. NEUTRON DIFFRACTION EXPERIMENTS

The *in situ* high-pressure neutron diffraction with isotope substitution measurements were made at pressures of 3.0(5), 4.7(5), 6.3(5), 7.1(5), and 8.2(5) GPa using the samples described in Refs. [8,11]. The diffractometer D4 (Ref. [29]) was employed using the experimental and data analysis procedures described in Refs. [20,30] but with an incident wavelength of 0.4961(1) Å to enhance the measured k range. Additionally, the structure of $^{N}Ge^{N}Se_2$ was investigated at 1.7(5), 3.0(5), 3.9(5), and 4.7(5) GPa by using D4, and at 8.7(5), 10.9(5), 12.8(5), 14.4(5), and 16.1(5) GPa by using the time-of-flight diffractometer PEARL.
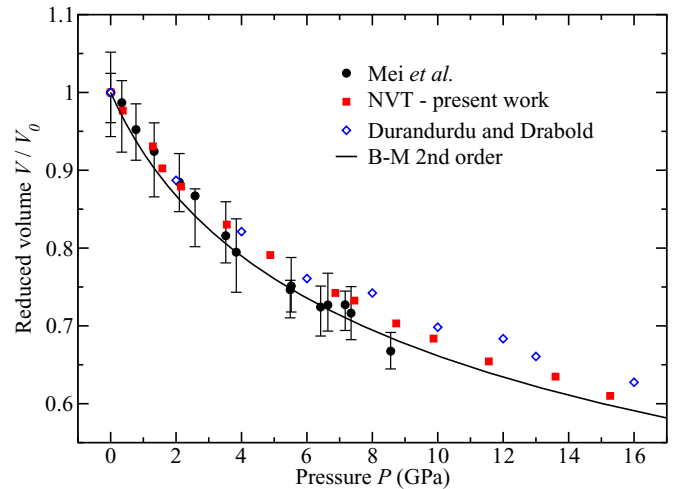

FIG. 1. (Color online) The pressure-volume equation of state for GeSe$_2$ glass under compression. The measured data from Mei *et al.* [17] [(black) ● with vertical error bars] are compared to the results obtained from FPMD in (i) this work using the BLYP functional [(red) ■] and (ii) the work by Durandurdu and Drabold [16] [(blue) ◇]. The measured data were fitted using a second-order Birch-Murnaghan equation of state [solid (black) curve].

The experimental and data analysis protocols associated with the latter are described in Ref. [31]. The neutron scattering lengths, taking into account the isotopic enrichments [8,11], are $b_{NGe} = 8.185(20)$, $b_{70Ge} = 10.0(1)$, $b_{73Ge} = 5.09(4)$, $b_{NSe} = 7.970(9)$, and $b_{76Se} = 12.2(1)$ fm [32].

The number density of GeSe$_2$ glass at ambient pressure was measured to be $\rho_0 = 0.0324(1)$ Å^{-3} by using a helium pycnometer. At pressures up to 8.5 GPa, ρ was taken from the measured pressure dependence of the reduced volume V/V_0 for GeSe$_2$ glass under cold compression (Fig. 1) [17], where V is the volume at pressure P and V_0 is the volume at ambient pressure. At higher pressures, ρ was taken from a fit to this experimental data using a second-order Birch-Murnaghan equation of state [33] $P = (3B_0/2)[(V/V_0)^{-7/3} - (V/V_0)^{-5/3}]$ which gives an isothermal bulk modulus $B_0 = 10.55(30)$ GPa. In comparison, a value $B_0 = 14.22(1.81)$ GPa is obtained by fitting to a third-order Birch-Murnaghan equation of state [17], and an adiabatic bulk modulus of 14.5 GPa (Ref. [34]) or 12.64 GPa (Ref. [35]) is obtained for Ge$_{30}$Se$_{70}$ glass from sound velocity measurements.

IV. FIRST-PRINCIPLES MOLECULAR DYNAMICS SIMULATIONS

The simulations used the Car-Parrinello [21] molecular dynamics method as implemented in the CPMD computer code (version 3.17) [36] with the *NVT* ensemble and $N = 120$ atoms. For most state points, the Becke-Lee-Yang-Parr (BLYP) functional [37,38] was used to describe the electron exchange and correlation. This functional was chosen because it leads to an accurate representation of the structure-related properties of several liquid and glassy Ge$_x$Se$_{1-x}$ ($0 \leqslant x \leqslant 1$) materials at ambient pressure [14,15,22–24]. Valence electrons were treated explicitly and were represented by a plane-wave basis set expanded at the Γ point of the simulation cell with

an energy cutoff of 20 Ry. The valence-core interactions were described by norm-conserving pseudopotentials of the Troullier-Martins type [39]. The largest cutoff used in the pseudopotential construction was equal to 1.06 Å. A fictitious electron mass of 1000 a.u. (i.e., in units of $m_e a_0^2$ where m_e is the electron mass and a_0 is the Bohr radius) and a time step of $\Delta t =$ 0.24 fs were used to integrate the equations of motion, ensuring good control of the conserved quantities. The temperature was controlled by a Nosé-Hoover thermostat [40,41].

The simulations were initiated from ambient P and T configurations with vanishing stress-tensor values [15] that gave best agreement with the measured partial structure factors [8,11]. The simulation for each new pressure started from a configuration taken from the previous (lower) pressure after the density was increased by decreasing the volume V. The system was then taken on a five-step thermal cycle, starting at $T = 300$ K for 40 ps, increasing to $T = 600$ K for 50 ps and then to $T = 900$ K for 150 ps, decreasing to $T = 600$ K for 70 ps, and finishing at $T = 300$ K for 150 ps [15]. The dwell time at each temperature could vary by ± 20 ps from one simulation to another, but the dwell times for the cooling part of a cycle were kept longer than for the heating part of a cycle to allow for relaxation. The total duration of a thermal cycle was in the 350–460 ps range. Substantial diffusion at $T = 900$ K on the scale of several interatomic distances ensured that no memory was kept of an initial configuration, and that the glasses produced under pressure were statistically uncorrelated. Statistical averages were taken from the final 50-ps portion of the relaxed $T = 300$ K trajectory at the end of a thermal cycle. For each pressure, 2–3 different configurations were considered. The modeled equation of state is in accord with experiment [17] within the measurement error (Fig. 1).

For a single state point at $V/V_0 = 0.654$ ($\rho/\rho_0 = 1.529$) a hybrid functional was used. The motivation for this switch was to improve the exchange-correlation term to see if this leads to a better reproduction of the experimental results at high pressure. Our specific choice of hybrid functional (Heyd-Scuseria-Ernzerhof HSE06) is a generalization of the PBE0 functional [42] proposed by the group of Scuseria [43], in which the Perdew-Burke-Ernzerhof (PBE) exchange functional [44] is complemented by the Hartree exact exchange with a properly calibrated mixing coefficient. We used the same CPMD setup to perform the HSE06 calculation. The only differences were (i) the use of a plane-wave basis set expanded at the Γ point of the simulation cell with an energy cutoff of 30 Ry, and (ii) the use of a four-step thermal cycle starting at $T = 300$ K for 1.2 ps, increasing to $T = 1100$ K for 3.4 ps, decreasing to $T = 900$ K for 5.8 ps, and finishing at $T = 300$ K for 6.6 ps. The results were obtained from analyzing the relaxed $T = 300$ K trajectory at the end of the thermal cycle. The FPMD simulations using the hybrid density functional are ~50 times slower than those using the BLYP functional.

In the following, the FPMD results from this work are those obtained by using the BLYP functional unless otherwise specified.

V. RESULTS

The difference functions measured using D4 at pressures up to 8.2(5) GPa are shown in Fig. 2 and the total structure factors measured using PEARL at higher pressures are shown
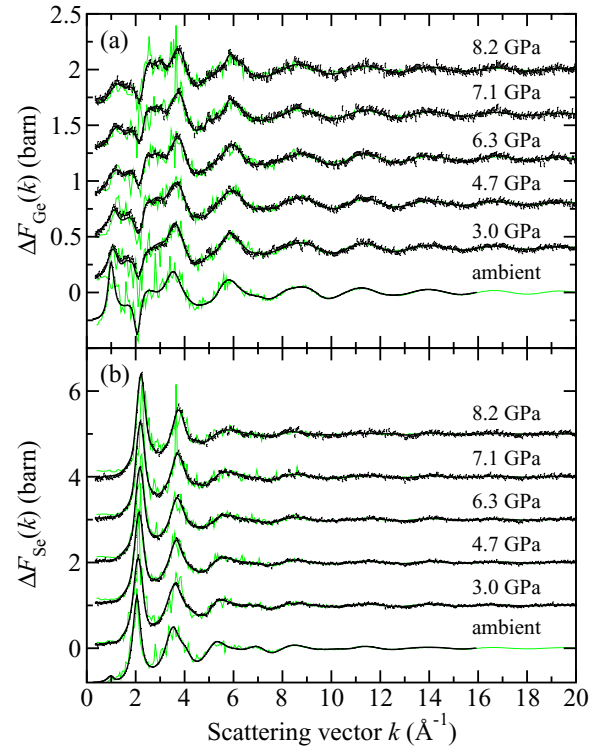

FIG. 2. (Color online) The difference functions (a) $\Delta F_{\text{Ge}}(k)/$ barn $= 0.236(4)[S_{\text{GeSe}}(k) - 1] + 0.099(2)[S_{\text{GeGe}}(k) - 1]$ and (b) $\Delta F_{\text{Se}}(k)/\text{barn} = 0.184(3)[S_{\text{GeSe}}(k) - 1] + 0.588(11)[S_{\text{SeSe}}(k) - 1]$ as measured using the diffractometer D4 at ambient pressure (Ref. [8]) and at pressures of 3.0(5), 4.7(5), 6.3(5), 7.1(5), and 8.2(5) GPa (points with vertical error bars). The data sets are compared to FPMD results at ambient pressure and at 3.4, 4.88, 7.25, 8.73, and 9.87 GPa [light (green) curves]. The dark (black) curves are the back Fourier transforms of the measured r-space difference functions shown in Fig. 4.

in Fig. 3(a). The corresponding real-space functions are shown in Figs. 4 and 3(b), respectively. The measured $G(r)$ functions in Fig. 3(b) were obtained by Fourier transforming the $F(k)$ functions shown in Fig. 3(a) before and after the application of a Lorch [27] modification function. The data obtained from the first procedure were then joined smoothly to the data obtained from the second procedure at a point just beyond the first peak in real space.

The measured mean nearest-neighbor bond distance $\bar{r}$ and coordination number $\bar{n}$ found from neutron diffraction are compared to the x-ray diffraction results of Mei *et al.* [17] in Figs. 5(a) and 5(b). To emphasize the density dependence of the structural transformations that occur, the data sets in Fig. 5 are plotted in terms of the reduced number density ρ/ρ_0, where ρ and ρ_0 are the values at high and ambient pressure, respectively. The neutron and x-ray diffraction $\bar{r}$ values are in agreement at all densities, but there is disagreement between the $\bar{n}$ values at higher densities. This discrepancy can, however, be eliminated by removing an unphysical slope on the x-ray total structure factors and renormalizing.

The FPMD results are compared to the diffraction data in Figs. 2–4. The data sets are matched according to their number density because the measured and simulated equations of state are not identical (Fig. 1). The simulations account for all of the
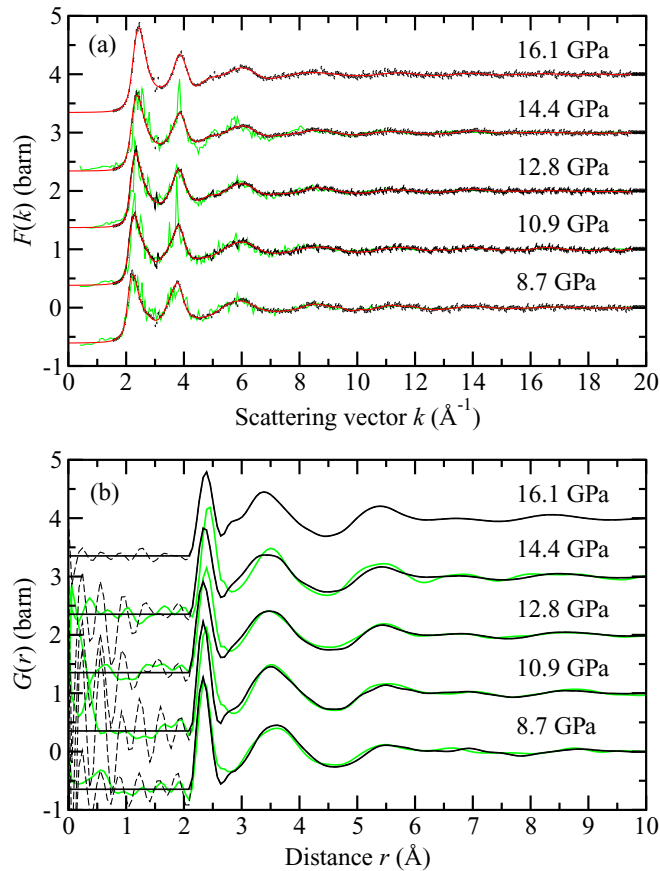
FIG. 3. (Color online) The pressure dependence of (a) the total structure factor $F(k)$ and (b) the total pair-distribution function $G(r)$ for $^{N}Ge^{N}Se_2$ glass. (a) The data sets measured using the PEARL diffractometer are given by the points with vertical error bars. The solid (red) curves show spline fits to these measured data sets, except when $k < 1.55$ Å^{-1} where they represent fitted Lorentzian functions because this region was not accessible in the diffraction experiments (see Ref. [31]). The solid light (green) curves show the FPMD results for pressures of 9.87, 11.56, 13.82, and 15.27 GPa. (b) The $G(r)$ functions shown by the solid (black) curves are the Fourier transforms of the measured $F(k)$ functions given in (a), and the broken (black) curves show the extent of the unphysical oscillations at r values smaller than the distance of closest approach between the centers of two atoms. The solid light (green) curves show the Fourier transforms of the simulated functions shown in (a) after applying the same maximum cutoff value $k_{max} = 19.55$ Å^{-1} as used for the neutron diffraction data.

main features in the measured difference functions at pressures up to 8.2(5) GPa. As shown in Figs. 5(a) and 5(b), they also give $\bar{r}$ and $\bar{n}$ values that are in agreement with experiment within the measurement error. At higher pressures, the measured and simulated results both show an increase in $\bar{n}$ as the first coordination shell expands to incorporate a larger number of neighbors. This process starts, however, at ~8.5 GPa from FPMD (ρ/ρ_0 ~1.42) as compared to ~12 GPa (ρ/ρ_0 ~1.55) from experiment.

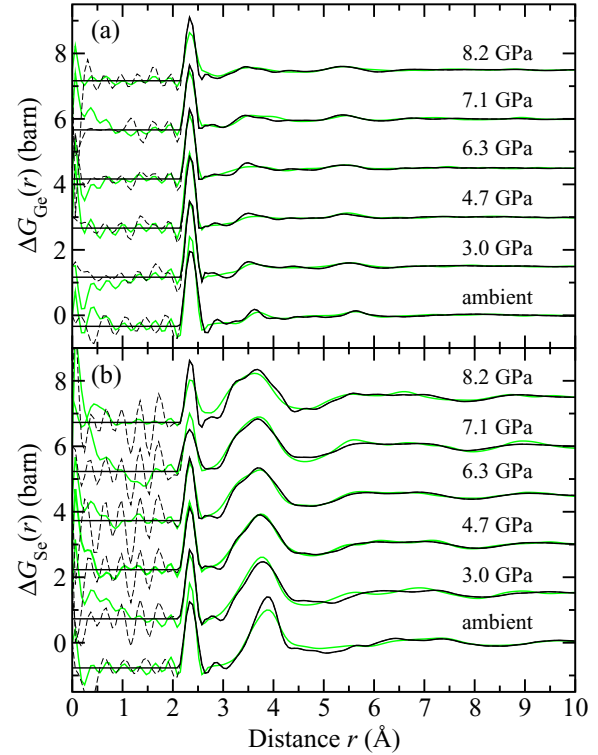We note that differences between the measured and simulated data sets can be assessed by using the goodness-of-fit

FIG. 4. (Color online) The pressure dependence of (a) $\Delta G_{Ge}(r)/$barn $= 0.236(4)[g_{GeSe}(r) - 1] + 0.099(2)[g_{GeGe}(r) - 1]$ and (b) $\Delta G_{Se}(r)/$barn $= 0.184(3)[g_{GeSe}(r) - 1] + 0.588(11)$ $[g_{SeSe}(r) - 1]$. The solid (black) curves were obtained by spline fitting and Fourier transforming the measured k-space functions shown in Fig. 2, and the broken curves show the extent of the unphysical oscillations at r values smaller than the distance of closest approach between the centers of two atoms. The light (green) curves give the Fourier transforms of the FPMD results shown in Fig. 2 after applying the same cutoff $k_{max} = 20.5$ Å^{-1} as used for the high-P diffraction data.

parameter [45]

$$R_\chi \equiv \left\{ \frac{\sum_i [T_{ND}(r_i) - T_{FPMD}(r_i)]^2}{\sum_i T_{ND}^2(r_i)} \right\}^{1/2}, \qquad (5)$$

where ND indicates a $T(r)$ function measured by neutron diffraction. At pressures up to 8.2 GPa, the R_χ parameter as calculated by taking $T(r) = 4\pi\rho r[\Delta G_{Ge/Se}(r) - \Delta G_{Ge/Se}(0)]$ (where the notation $\Delta G_{Ge/Se}(r)$ implies either the $\Delta G_{Ge}(r)$ or $\Delta G_{Se}(r)$ function) is 9.4% at ambient and 4.3%–4.8% at higher pressures for the data sets shown in Fig. 4(a), or is 12.2% at ambient and 5.4%–11.0% at higher pressures for the data sets shown in Fig. 4(b). The R_χ parameter as calculated by taking $T(r) = 4\pi\rho r[G(r) - G(0)]$ changes from 4.5% at 8.7 GPa to 8.2% at 14.4 GPa for the data sets shown in Fig. 3(b). All of these R_χ values correspond to an r-space interval of 2–10 Å.

The ρ/ρ_0 dependence of the fractions of n-fold coordinated Ge and Se atoms ($n = 2, 3, 4, 5,$ or 6) obtained from the FPMD simulations is given in Figs. 5(c) and 5(d), and is broken down in Figs. 5(e) and 5(f) into the proportions of these n-fold species that contain homopolar bonds. As
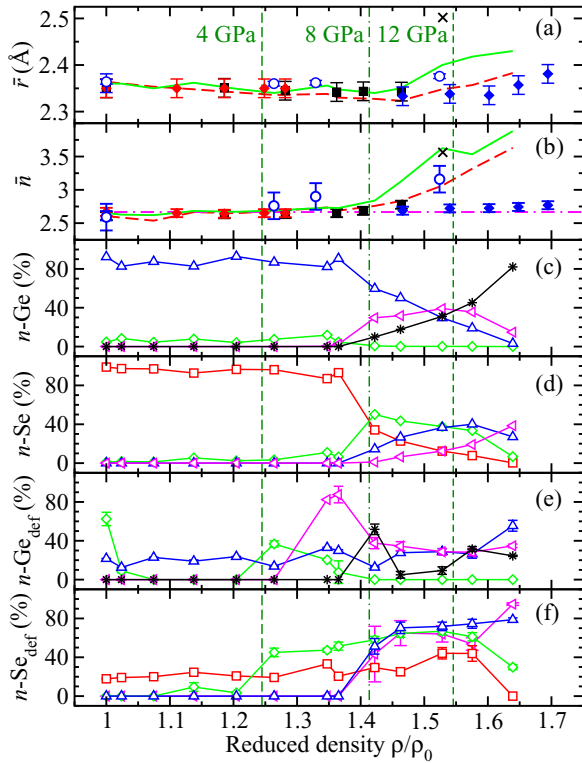
FIG. 5. (Color online) The ρ/ρ_0 dependence of the nearest-neighbor (a) bond distance $\bar{r}$ and (b) coordination number $\bar{n}$ as obtained from (i) neutron diffraction using a $^N Ge^N Se_2$ sample on either the D4 [(red) ♦] or PEARL [(blue) ♦] diffractometer, or using $^{70}Ge^N Se_2$ and $^{73}Ge^{76}Se_2$ samples and averaging the results [(black) ■]; (ii) x-ray diffraction [17] [(blue) ○]; (iii) FPMD [solid (green) curves] where the results obtained before the high-temperature anneal at each pressure point are also given [broken (red) curves]; and (iv) FPMD (×) performed by using the HSE06 hybrid functional. $\bar{n}$ was found from the simulated $\bar{n}_\alpha^\beta$ values by using a cutoff distance specified by the first minimum in $G(r)$. In (b), the horizontal chained line gives the "8-N" rule expectation of $\bar{n} = 2.67$ [12]. Also given are the FPMD results for the fractions of n-fold coordinated (c) Ge and (d) Se atoms, along with the fractions of these n-fold coordinated (e) Ge and (f) Se atoms that have homopolar bonds. In (c)–(f), the symbols denote twofold [(red) □], threefold [(green) ◇], fourfold [(blue) △], fivefold [(magenta) ◁], or sixfold [(black) ∗] coordinated species, and the error bars (usually smaller than the symbol size) were calculated according to Ref. [13]. The vertical broken lines correspond to pressures of ~4, 8, and 12 GPa.

the density is increased to $\rho/\rho_0 \sim 1.55$, there is no obvious tendency for a suppression of chemical disorder as suggested by previous work [16]. The simulated intrapolyhedral Se-Ge-Se and interpolyhedral Ge-Se-Ge bond angle distributions $P(\theta_{SeGeSe}) = B(\theta_{SeGeSe})/\sin(\theta_{SeGeSe})$ and $P(\theta_{GeSeGe}) = B(\theta_{GeSeGe})/\sin(\theta_{GeSeGe})$ are shown in Figs. 6(a) and 6(b), where the distributions $B(\theta)$ are normalized by $\sin(\theta)$ to remove the effect of a finite sampling volume [46]. The fractions of Ge atoms that are involved either in CS or ES motifs are given in Fig. 6(c). The CS motifs are denoted by Ge_0 while the ES motifs are broken down into their contributions from Ge_ℓ ($\ell = 1, 2, 3/4$) centered polyhedra, where ℓ indicates the number of ES connections to other polyhedra and $\ell = 3/4$ denotes three or four of these connections.
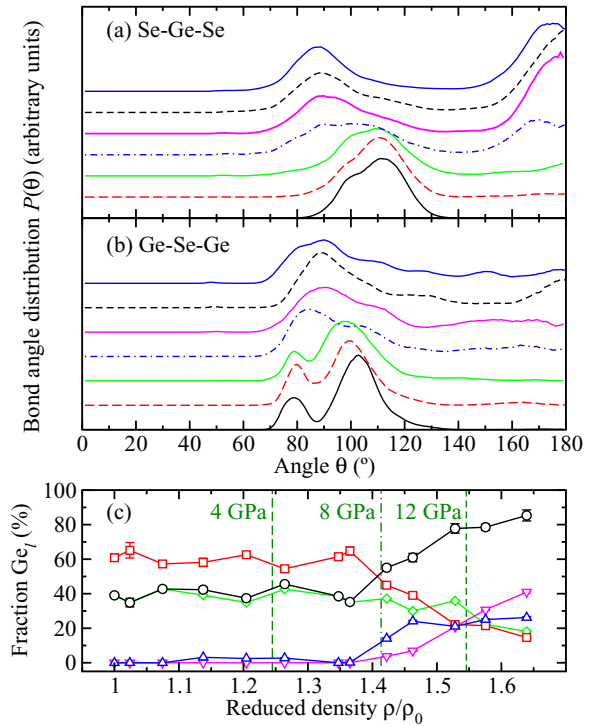

FIG. 6. (Color online) FPMD results showing the ρ/ρ_0 dependence of (a) the intrapolyhedral Se-Ge-Se and (b) the interpolyhedral Ge-Se-Ge bond angle distributions where, from bottom to top in each panel, $\rho/\rho_0 = 1$, 1.204, 1.365, 1.463, 1.528, 1.575, or 1.639. In (c), the density dependence of the fractions of CS Ge atoms (Ge_0, □) and ES Ge atoms (○) is given, together with a breakdown of the latter into its contributions from Ge_1 (◇), Ge_2 (△), and $Ge_{3/4}$ (▽) units. In (c), the error bars (usually smaller than the symbol size) were calculated according to Ref. [13], and the vertical broken lines correspond to pressures of ~4, 8, and 12 GPa.

Figure 7 shows the ρ/ρ_0 dependence of the mean Se-Ge-Se and Ge-Se-Ge bond angles as estimated from the measured Ge-Se, Ge-Ge, and Se-Se distances using the cosine rule, namely, $\cos(\theta_{SeGeSe}) = 1 - r_{SeSe}^2/2r_{GeSe}^2$ and $\cos(\theta_{GeSeGe}) = 1 - r_{GeGe}^2/2r_{GeSe}^2$. The distance r_{GeSe} was taken from the mean of the first peak positions in (i) the total pair-distribution function $G(r)$ for the $^{70}Ge^N Se_2$ and $^{73}Ge^{76}Se_2$ samples and (ii) the first-difference functions $\Delta G_{Ge}(r)$ and $\Delta G_{Se}(r)$. The distance r_{SeSe} was taken from the second peak in $\Delta G_{Se}(r)$ which is dominated by the Se-Se partial pair-distribution function: The ratio of weighting factors for the Se-Se:Ge-Se partial pair-distribution functions is 1:0.3129. The distance r_{GeGe} was estimated from the second peak in $\Delta G_{Ge}(r)$ where the ratio of weighting factors for the Ge-Ge:Ge-Se partial pair-distribution functions is 1:2.3838. The measured results, which correspond to the pressure interval from ambient to 8.2 GPa, are compared to the mean bond angles $\langle\theta_{SeGeSe}\rangle$ and $\langle\theta_{GeSeGe}\rangle$ obtained from the FPMD bond angle distributions $P(\theta)$ [several of the latter are shown in Figs. 6(a) and 6(b)]. The expression $\langle\theta\rangle = \int d\theta\, \theta\, P(\theta)/\int d\theta\, P(\theta)$ was used with a high-angle integration cutoff of $140°$. The Se-Se distance can be accurately discerned from the measured first-difference function $\Delta G_{Se}(r)$ and the ρ/ρ_0 dependence of the simulated $\langle\theta_{SeGeSe}\rangle$ values tracks that found from experiment. It is,
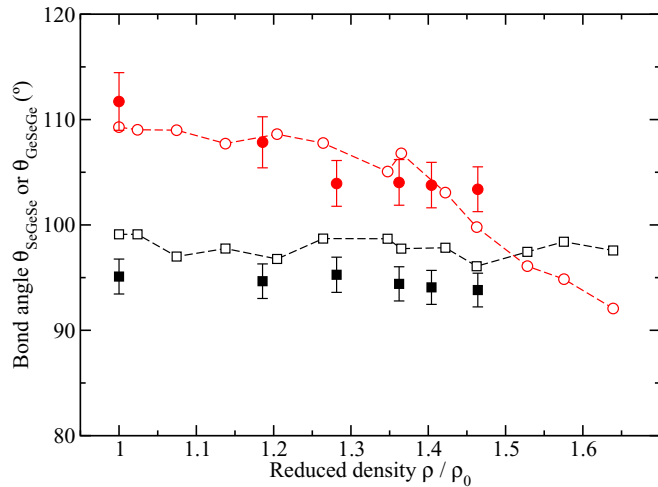
FIG. 7. (Color online) The ρ/ρ_0 dependence of the mean intra-polyhedral Se-Ge-Se [(red) ● with vertical error bars] and inter-polyhedral Ge-Se-Ge [(black) ■ with vertical error bars] bond angles as estimated from the measured Ge-Se, Ge-Ge and Se-Se distances (see the text). The experimental results are compared to the mean values $\langle\theta_{SeGeSe}\rangle$ [broken (red) curve with ○ symbols] and $\langle\theta_{GeSeGe}\rangle$ [broken (black) curve with □ symbols] taken from the FPMD simulations.

however, more difficult to discern the Ge-Ge distance from the measured first-difference function $\Delta G_{Ge}(r)$ and there is an offset between the measured and simulated Ge-Se-Ge bond angles, although both data sets show the same ρ/ρ_0 dependence.

VI. DISCUSSION

The following picture emerges from the measured and FPMD results for a two-stage densification process in GeSe$_2$ glass. In the first stage where the diffraction and FPMD results are in accord, $\bar{n}$ remains constant as the density increases from ambient to $\rho/\rho_0 \sim 1.42$. The CS to ES ratio increases from 1.3 to 1.7 in the interval $\rho/\rho_0 \sim 1.07$–1.20 ($P \sim 1.29$–3.55 GPa) [Fig. 6(c)], consistent with the trend found from Raman spectroscopy [47]. The results do not, however, support the model of Antao *et al.* [48] where an increase of $\bar{n}$ was invoked to explain a minimum in the network rigidity at $\simeq 4$ GPa ($\rho/\rho_0 \simeq 1.25$). The prevalence of ES units contrasts to the crystalline phase where transitions are observed from an ambient-pressure two-dimensional (2D) structure comprising equal numbers of ES and CS tetrahedra [49] to three-dimensional (3D) structures of densely packed CS tetrahedra [50,51]. Higher temperatures are, however, usually required to facilitate these transitions [50–53].

In the second stage, as the density is increased beyond $\rho/\rho_0 \sim 1.42$, $\bar{n}$ increases with $\bar{r}$ although there is a discrepancy between the rate of change found from diffraction and FPMD. In the latter, fourfold coordinated Ge atoms make way for fivefold and sixfold coordinated Ge atoms [Fig. 5(c)], twofold coordinated Se atoms make way for higher-coordinated Se atoms [Fig. 5(d)] where homopolar bonds are common [Fig. 5(f)], and there is a monotonic reduction in the CS to ES ratio [Fig. 6(c)]. The FPMD results for $\bar{n}$ indicate a

bonding scheme that takes an increased metallic character with increasing pressure, whereas the diffraction results are consistent with the retention of semiconducting behavior.

In an attempt to improve the agreement between simulation and experiment, we performed an additional FPMD simulation at $\rho/\rho_0 = 1.529$ by using a hybrid functional of the HSE06 type (Sec. IV) [43]. The aim was to determine whether or not inclusion of the Hartree exact exchange is capable of retaining to higher pressures a more ionic and less metallic character for the chemical bonding [54]. The calculations did not, however, lead to improved agreement with experiment [Figs. 5(a) and 5(b)]. The origin of the discrepancy may therefore lie with the exploration of different pathways of metastability: The glass was cold compressed in the diffraction experiments but was annealed at a high temperature of 900 K at high pressure in the FPMD simulations (Sec. IV). The effect of the high-T anneal at a given pressure point can be illustrated by analyzing the configurations obtained at the end of the preceding low-T anneal at 300 K. The rate of change of $\bar{r}$ and $\bar{n}$ with density is reduced when $\rho/\rho_0 > 1.42$ [Figs. 5(a) and 5(b)]. The results therefore indicate the presence of an energy barrier to structural transformation within the high-pressure regime that is partially surmounted by the high-T anneal at 900 K. In other words, a single valley in the energy landscape at pressures up to ~ 8.5 GPa ($\rho/\rho_0 \sim 1.42$) bifurcates at higher pressures to give two valleys separated by an energy barrier that can be overcome by heating to a temperature of ~ 900 K.

Figure 8 shows typical atomistic configurations from FPMD for different points in the densification process. When ρ/ρ_0 increases beyond 1.42, the Se atoms in Ge$_0$ motifs make additional bonds with their neighboring Ge$_1$ motifs, transforming the latter to fivefold coordinated Ge$_2$ units having a distorted square pyramidal geometry. As Ge$_0$ tetrahedra are removed, the Se-Ge-Se bond angle distribution broadens, its peak shifts from $\sim 111°$ towards smaller angles, and there is a merger of the twin peaks in the Ge-Se-Ge bond angle distribution [Figs. 6(a) and 6(b)]. Around $\rho/\rho_0 \simeq 1.53$, the fraction of Ge$_0$ units continues to decrease, making way for more Ge$_2$ and a few Ge$_{3/4}$ type configurations, where many of the latter correspond to sixfold coordinated Ge atoms. Accordingly, the main peak in the Se-Ge-Se bond angle distribution shifts to around
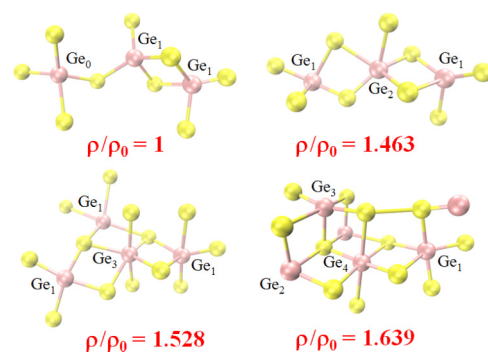

FIG. 8. (Color online) Atomistic configurations from FPMD for GeSe$_2$ glass at different reduced densities. Ge atoms are dark (purple) and Se atoms are light (yellow). Bonds are drawn when two atoms are separated by a distance $\leqslant r_{min}$ given by the position of the first minimum in $g_{GeSe}(r)$.

$90°$ and a second peak appears near $180°$. Eventually, the network develops a pseudocubic arrangement of Ge-centered units for which the main peak in the Ge-Se-Ge bond angle distribution is at $\sim 90°$. In all of this, the fractions of defected fivefold and sixfold coordinated Ge atoms peak at densities around which these species first start to emerge [Fig. 5(e)], i.e., homopolar bonds mediate in the initial development of the higher-coordinated Ge-centered polyhedra.

It is also illustrative to follow the transformations of the Ge-centered structural motifs in terms of the q parameter defined by $q \equiv 1 - (3/8) \sum_{k>i} [(1/3) + \cos \theta_{ijk}]^2$, where θ_{ijk} is the angle formed between a central Ge atom j and its neighboring atoms i and k [55,56]. The parameter $q = 1$ if the Ge atom is at the center of a regular tetrahedron, $q = 0$ if it is at the center of a regular octahedron, or $q = 53/96 = 0.552$ if it is at the center of a trigonal bipyramid. In comparison, for a square pyramidal unit in which the central fivefold coordinated Ge atom is located at the base center then $q = \frac{1}{3}$. Alternatively, if this Ge atom is displaced toward the apex by a distance $h/5$, where h is the base-to-apex distance, then (i) $q = 0.504$ if all of the edges are equal in length (corresponding, e.g., to equal Se-Se distances in a GeSe$_5$ unit) or (ii) $q = 0.535$ if h is elongated relative to (i) to give the central Ge atom equal nearest-neighbor distances [57]. Figure 9 shows the ρ/ρ_0 dependence of the q-parameter distributions obtained from the FPMD simulations of GeSe$_2$ glass. At ambient conditions, most of the Ge atoms are fourfold coordinated in distorted tetrahedral units with a maximum in the distribution at $q \simeq 0.966$. In comparison, the mean q value is 0.979 for the high-temperature ambient-pressure crystalline phase of GeSe$_2$ [49]. At higher densities, most of the fivefold coordinated Ge atoms appear in distorted square-pyramidal (as opposed to trigonal bipyramidal) conformations. The majority of sixfold coordinated Ge atoms are in distorted octahedral environments which give rise to a sharp peak at a small negative q value.
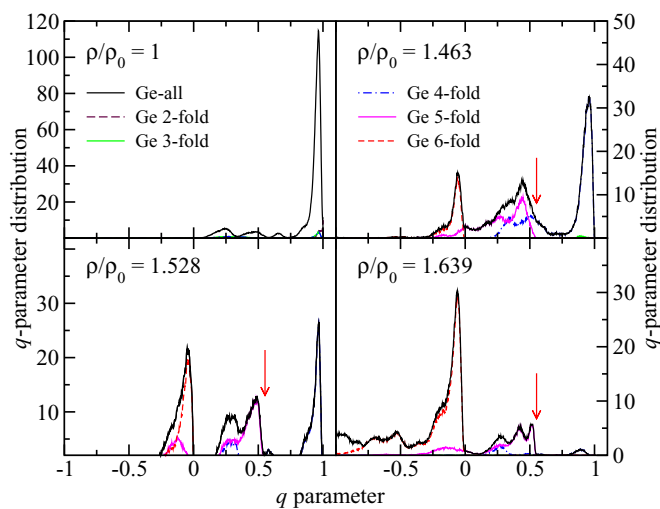

FIG. 9. (Color online) The ρ/ρ_0 dependence of the q-parameter distribution as obtained from the FPMD simulations of GeSe$_2$ glass. At each density, the distribution for all Ge atoms is broken down into its contributions from n-fold coordinated Ge atoms ($n = 3$, 4, 5, or 6). The vertical (red) arrows mark the q value expected for trigonal bipyramidal units.

VII. CONCLUSIONS

In the range from ambient pressure to $P \sim 8.5$ GPa ($1 \leqslant \rho/\rho_0 \leqslant 1.42$) there is excellent agreement between the neutron diffraction and FMPD results that extends from the profiles of the measured difference functions (Figs. 2 and 4) to the mean nearest-neighbor bond distance $\bar{r}$ [Fig. 5(a)], coordination number $\bar{n}$ [Fig. 5(b)], and Se-Ge-Se bond angle (Fig. 7). For this regime, the ambient-pressure $\bar{n}$ value is retained, and the density-driven structural transformations in GeSe$_2$ differ substantially from those observed in common oxide glasses such as SiO$_2$, GeO$_2$, and B$_2$O$_3$. In particular, ES motifs remain numerous, in contrast to oxide glasses where CS conformations dominate over the density range where the chemical species retain their ambient-pressure coordination numbers [20,58–63].

At larger pressures, however, the diffraction and FPMD results diverge. In particular, the diffraction results show a slow increase in $\bar{r}$ and $\bar{n}$ with pressure which suggests the retention of semiconducting behavior to higher densities than found by FPMD. In the latter, densification proceeds by the formation of fivefold and sixfold coordinated Ge atoms, leading to larger fractions of ES polyhedra, along with threefold, fourfold, and fivefold coordinated Se atoms. On initial formation, large proportions of the higher-coordinated Ge and Se atoms have homopolar bonds, i.e., these defects mediate in the density-driven structural transformations. This feature is in contrast to oxides where chemical ordering is preferred at all pressures [20,58–63].

The discrepancy between the neutron diffraction and FPMD results at high pressure is attributed to the presence of an energy barrier to structural rearrangement, which cannot be explored in the cold-compression diffraction experiments but can be accessed via the high-temperature annealing stage in the simulations. In other words, a single valley in the energy landscape at pressures up to ~ 8.5 GPa ($\rho/\rho_0 \sim 1.42$) bifurcates at higher pressures to give two valleys separated by an energy barrier that can be surmounted by heating to a temperature of ~ 900 K. It is a moot point as to whether structural relaxation at high temperature in the simulations is enabling access to crystallinelike configurations: A discontinuous semiconductor-glass to metal-crystalline transition has been reported for GeSe$_2$ at $P \simeq 7$ GPa [18,19].

Notwithstanding, the stability under load of ES tetrahedra, which promote the fragility of glass-forming liquids [64], and the importance of homopolar bonds in mediating the transformations to higher-coordinated polyhedra, are likely to be common features in the mechanisms of network collapse for the class of glass-forming materials where these motifs are prevalent in the ambient-pressure networks.

[1] V. V. Brazhkin and A. G. Lyapin, J. Phys.: Condens. Matter **15**, 6059 (2003).

[2] M. C. Wilding, M. Wilson, and P. F. McMillan, Chem. Soc. Rev. **35**, 964 (2006).

[3] Z. U. Borisova, *Glassy Semiconductors* (Plenum, New York, 1981).

[4] A. Sartbaeva, S. A. Wells, A. Huerta, and M. F. Thorpe, Phys. Rev. B **75**, 224204 (2007).

[5] C. Massobrio, M. Celino, P. S. Salmon, R. A. Martin, M. Micoulaut, and A. Pasquarello, Phys. Rev. B **79**, 174201 (2009).

[6] P. Boolchand, J. Grothaus, W. J. Bresser, and P. Suranyi, Phys. Rev. B **25**, 2975 (1982).

[7] M. Cobb, D. A. Drabold, and R. L. Cappelletti, Phys. Rev. B **54**, 12162 (1996).

[8] I. Petri, P. S. Salmon, and H. E. Fischer, Phys. Rev. Lett. **84**, 2413 (2000).

[9] P. Boolchand and W. J. Bresser, Philos. Mag. B **80**, 1757 (2000).

[10] X. Zhang and D. A. Drabold, Phys. Rev. B **62**, 15695 (2000).

[11] P. S. Salmon and I. Petri, J. Phys.: Condens. Matter **15**, S1509 (2003).

[12] P. S. Salmon, J. Non-Cryst. Solids **353**, 2959 (2007).

[13] C. Massobrio and A. Pasquarello, Phys. Rev. B **77**, 144207 (2008).

[14] C. Massobrio, M. Micoulaut, and P. S. Salmon, Solid State Sci. **12**, 199 (2010).

[15] A. Bouzid and C. Massobrio, J. Chem. Phys. **137**, 046101 (2012).

[16] M. Durandurdu and D. A. Drabold, Phys. Rev. B **65**, 104208 (2002).

[17] Q. Mei, C. J. Benmore, R. T. Hart, E. Bychkov, P. S. Salmon, C. D. Martin, F. M. Michel, S. M. Antao, P. J. Chupus, P. L. Lee, S. D. Shastri, J. B. Parise, K. Leinenweber, S. Amin, and J. L. Yarger, Phys. Rev. B **74**, 014203 (2006).

[18] S. Asokan, M. V. N. Prasad, G. Parthasarathy, and E. S. R. Gopal, Phys. Rev. Lett. **62**, 808 (1989).

[19] M. V. N. Prasad, S. Asokan, G. Parthasarathy, S. S. K. Titus, and E. S. R. Gopal, Phys. Chem. Glasses **34**, 199 (1993).

[20] K. Wezka, P. S. Salmon, A. Zeidler, D. A. J. Whittaker, J. W. E. Drewitt, S. Klotz, H. E. Fischer, and D. Marrocchelli, J. Phys.: Condens. Matter **24**, 502101 (2012).

[21] R. Car and M. Parrinello, Phys. Rev. Lett. **55**, 2471 (1985).

[22] M. Micoulaut, R. Vuilleumier, and C. Massobrio, Phys. Rev. B **79**, 214205 (2009).

[23] S. Le Roux, A. Zeidler, P. S. Salmon, M. Boero, M. Micoulaut, and C. Massobrio, Phys. Rev. B **84**, 134203 (2011).

[24] S. Le Roux, A. Bouzid, M. Boero, and C. Massobrio, Phys. Rev. B **86**, 224201 (2012).

[25] M. Wilson, B. K. Sharma, and C. Massobrio, J. Chem. Phys. **128**, 244505 (2008).

[26] H. E. Fischer, A. C. Barnes, and P. S. Salmon, Rep. Prog. Phys. **69**, 233 (2006).

[27] E. Lorch, J. Phys. C: Solid State Phys. **2**, 229 (1969).

[28] P. S. Salmon, J. Phys.: Condens. Matter **18**, 11443 (2006).

[29] H. E. Fischer, G. J. Cuello, P. Palleau, D. Feltin, A. C. Barnes, Y. S. Badyal, and J. M. Simonson, Appl. Phys. A **74**, s160 (2002).

[30] J. W. E. Drewitt, P. S. Salmon, A. C. Barnes, S. Klotz, H. E. Fischer, and W. A. Crichton, Phys. Rev. B **81**, 014202 (2010).

[31] P. S. Salmon, J. W. E. Drewitt, D. A. J. Whittaker, A. Zeidler, K. Wezka, C. L. Bull, M. G. Tucker, M. C. Wilding, M. Guthrie, and D. Marrocchelli, J. Phys.: Condens. Matter **24**, 415102 (2012).

[32] V. F. Sears, Neutron News **3**, 26 (1992).

[33] F. Birch, Phys. Rev. **71**, 809 (1947).

[34] R. Ota, T. Yamate, N. Soga, and M. Kunugi, J. Non-Cryst. Solids **29**, 67 (1978).

[35] J.-P. Guin, T. Rouxel, J.-C. Sangleboeuf, I. Melscoët, and J. Lucas, J. Am. Ceram. Soc. **85**, 1545 (2002).

[36] http://www.cpmd.org

[37] A. D. Becke, Phys. Rev. A **38**, 3098 (1988).

[38] C. Lee, W. Yang, and R. G. Parr, Phys. Rev. B **37**, 785 (1988).

[39] N. Troullier and J. L. Martins, Phys. Rev. B **43**, 1993 (1991).

[40] S. Nosé, Mol. Phys. **52**, 255 (1984).

[41] W. G. Hoover, Phys. Rev. A **31**, 1695 (1985).

[42] C. Adamo and V. Barone, J. Chem. Phys. **110**, 6158 (1999).

[43] A. V. Krukau, O. A. Vydrov, A. F. Izmaylov, and G. E. Scuseria, J. Chem. Phys. **125**, 224106 (2006).

[44] J. P. Perdew, K. Burke, and M. Ernzerhof, Phys. Rev. Lett. **77**, 3865 (1996).

[45] A. C. Wright, J. Non-Cryst. Solids **159**, 264 (1993).

[46] A. Zeidler, P. S. Salmon, R. A. Martin, T. Usuki, P. E. Mason, G. J. Cuello, S. Kohara, and H. E. Fischer, Phys. Rev. B **82**, 104208 (2010).

[47] F. Wang, S. Mamedov, P. Boolchand, B. Goodman, and M. Chandrasekhar, Phys. Rev. B **71**, 174201 (2005).

[48] S. M. Antao, C. J. Benmore, B. Li, L. Wang, E. Bychkov, and J. B. Parise, Phys. Rev. Lett. **100**, 115501 (2008).

[49] G. Dittmar and H. Schäfer, Acta Crystallogr. B **32**, 2726 (1976).

[50] A. Grzechnik, S. Stølen, E. Bakken, T. Grande, and M. Mezouar, J. Solid State Chem. **150**, 121 (2000).

[51] T. Grande, M. Ishii, M. Akaishi, S. Aasland, H. Fjellvåg, and S. Stølen, J. Solid State Chem. **145**, 167 (1999).

[52] M. Shimada and F. Dachille, Inorg. Chem. **16**, 2094 (1977).

[53] L. F. Kulikova, L. M. Lityagina, I. P. Zibrov, T. I. Dyuzheva, N. A. Nikolaev, and V. V. Brazhkin, Inorg. Mater. **50**, 768 (2014).

[54] K. Y. Kim, D.-Y. Cho, B. Cheong, D. Kim, H. Horii, and S. Han, J. Appl. Phys. **113**, 134302 (2013).

[55] P.-L. Chau and A. J. Hardwick, Mol. Phys. **93**, 511 (1998).

[56] J. R. Errington and P. G. Debenedetti, Nature (London) **409**, 318 (2001).

[57] L. B. Skinner, A. C. Barnes, P. S. Salmon, L. Hennet, H. E. Fischer, C. J. Benmore, S. Kohara, J. K. Richard Weber, A. Bytchkov, M. C. Wilding, J. B. Parise, T. O. Farmer, I. Pozdnyakova, S. K. Tumber, and K. Ohara, Phys. Rev. B **87**, 024201 (2013).

[58] L. P. Dávila, M.-J. Caturla, A. Kubota, B. Sadigh, T. Diaz de la Rubia, J. F. Shackelford, S. H. Risbud, and S. H. Garofalini, Phys. Rev. Lett. **91**, 205501 (2003).

[59] S. K. Lee, P. J. Eng, H.-K. Mao, Y. Meng, M. Newville, M. Y. Hu, and J. Shu, Nat. Mater. **4**, 851 (2005).

[60] Y. Liang, C. R. Miranda, and S. Scandolo, Phys. Rev. B **75**, 024205 (2007).

[61] D. Marrocchelli, M. Salanne, and P. A. Madden, J. Phys.: Condens. Matter **22**, 152102 (2010).

[62] A. Zeidler, K. Wezka, D. A. J. Whittaker, P. S. Salmon, A. Baroni, S. Klotz, H. E. Fischer, M. C. Wilding, C. L. Bull, M. G. Tucker, M. Salanne, G. Ferlat, and M. Micoulaut, Phys. Rev. B **90**, 024206 (2014).

[63] A. Zeidler, K. Wezka, R. F. Rowlands, D. A. J. Whittaker, P. S. Salmon, A. Polidori, J. W. E. Drewitt, S. Klotz, H. E. Fischer, M. C. Wilding, C. L. Bull, M. G. Tucker, and M. Wilson (unpublished).

[64] M. Wilson and P. S. Salmon, Phys. Rev. Lett. **103**, 157801 (2009).